ELSEVIER

Materials Science and Engineering A 422 (2006) 19–28

MATERIALS SCIENCE & ENGINEERING A

www.elsevier.com/locate/msea

Pressure-balance and diffuse-interface models for surficial amorphous films

Jian Luo [a], Ming Tang [b], Rowland M. Cannon [c], W. Craig Carter [b], Yet-Ming Chiang [b,*]

[a] *School of Materials Science and Engineering and Center for Optical Materials Science and Engineering Technologies, Clemson University, Clemson, SC, USA*
[b] *Department of Materials Science and Engineering, Massachusetts Institute of Technology, Cambridge, MA, USA*
[c] *Lawrence Berkeley National Laboratory, University of California, Berkeley, CA, USA*

Received in revised form 25 November 2005

Abstract

Recent observations of nanoscale surficial amorphous films in Bi_2O_3-doped ZnO are briefly reviewed. The experimental results are modeled with two approaches. A pressure-balance model with the volumetric free energy being the dominant temperature-dependent interaction extended from Clarke's intergranular films model is proposed and numerically evaluated. This quantitative model predicts thicknesses versus temperature behavior for subeutectic films consistent with experimental results. Alternatively, the sequence of adsorption and wetting events as a function of temperature and composition is interpreted as a case of combined surface prewetting and premelting in a two-component system with a bulk eutectic reaction as a generalization of Cahn's critical point wetting model. In this second approach that better represents the through-thickness gradients, diffuse-interface formulation is proposed and analyzed for assessing surficial film stability as well as associated drying and complete wetting transitions. The observation made for Bi_2O_3 on ZnO can be represented by one of the possible surface prewetting/premelting phase diagrams.

Keywords: Surficial amorphous films; Intergranular amorphous films; Multilayer adsorption; Prewetting; Premelting; Diffuse interface

1. Introduction

A unique class of grain boundary wetting and adsorption behaviors has been observed in multicomponent ionic and covalent materials such as Si_3N_4, SiC, and ZnO doped with various additives, wherein an intergranular film (IGF) is stabilized at a nearly constant thickness on the order of 1 nm [1–10]. These IGFs can be alternatively understood to be liquid-like layers that adopt an "equilibrium thickness" in response to a balance among several specific interactions that may individually act to thicken or thin the film (Clarke [1]), or discrete and disordered multilayer adsorbates with compositions set by the bulk chemical potentials (Cannon and Esposito [3]). The physical basis of the formation and stability of IGFs is an open scientific question [1–5]. Furthermore, IGFs are technologically important [6–10].

Most recently, nanometer-thick, disordered intergranular films of similar character have been observed, surprisingly, in a model metallic system W–Ni [11]. This new observation shows the ubiquitous existence of this class of interfacial phenomena and provides new insights to understand the formation mechanism of these nanoscale interfacial films.

On the other hand, nanoscale films of similar character have recently been observed to form on free surfaces in several oxide systems [12–15], and for native oxide films on silicon surfaces under controlled ultra-low oxygen activities [16]. These films are termed surficial amorphous films (SAFs) despite indications of some local order existing within them [15]. A representative high-resolution transmission electron microscopy (HRTEM) image for an SAF observed in Bi_2O_3-doped ZnO is shown in Fig. 1. The formation of SAFs is analogous to the theories of equilibrium IGFs [1–3], multilayer gas adsorption [17], prewetting [18–23], and premelting [24–26], but none of the existing theories can be readily applied to explain the stability and character of these SAFs. In this paper we briefly summarize prior experimental observations of SAFs in the model system Bi_2O_3 on ZnO, and then present and discuss two theoretical models for these SAFs.

2. Summary of observations of SAFs in Bi_2O_3-doped ZnO [12–15]

Amongst all oxide systems studied, Bi_2O_3-doped ZnO have been mostly extensively characterized. The majority of our prior

* Corresponding author. Tel.: +1 617 253 6471; fax: +1 617 253 6201.
E-mail address: ychiang@mit.edu (Y.-M. Chiang).

0921-5093/$ – see front matter © 2006 Elsevier B.V. All rights reserved.
doi:10.1016/j.msea.2006.01.001

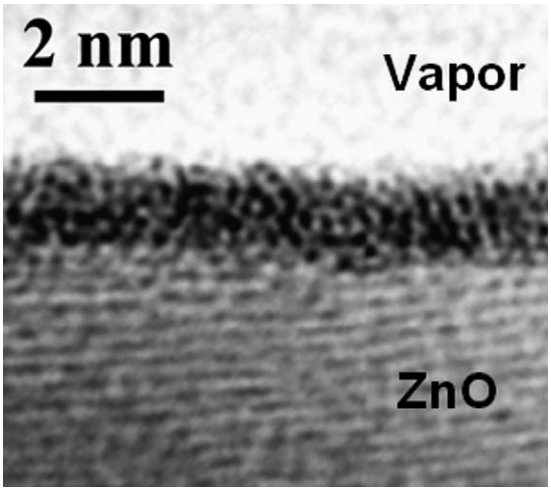

Fig. 1. A Bi_2O_3-enriched surficial amorphous film, or SAF, observed on the ZnO $\{1\,1\,\bar{2}\,0\}$ facet.

investigations were conducted via a powder experiment [12–15] wherein nano-sized, Bi_2O_3-doped ZnO powders were fired at elevated temperatures in closed containers to achieve thermal equilibration, air-quenched, and characterized by HRTEM. The observed SAFs in ZnO–Bi_2O_3 form preferentially on the $\{1\,1\,\bar{2}\,0\}$ surfaces. The anisotropic film formation has been attributed to induced order between the ZnO $\{1\,1\,\bar{2}\,0\}$ surface and bismuth oxide structural units constituting the film, which may lower the crystal–film interfacial energy and stabilize the surficial film [13]. The experimental observations of Bi_2O_3-enriched SAFs formed on ZnO $\{1\,1\,\bar{2}\,0\}$ surfaces are reported in Refs. [12–15], and briefly summarized as follows:

(i) Surficial films with similar character are observed in Bi_2O_3-saturated samples equilibrated above and below the bulk eutectic temperature, 740 °C, and in single-phase samples containing concentrations of Bi_2O_3 below the solid-solubility limit (Fig. 2(a)) [12–15].

(ii) These films have nearly constant thickness at a fixed temperature and chemical potential; once an equilibrium state has been reached, variations in additional annealing time and the amount of bulk second phase have no discernible influence on the average value of, or variability in, film thickness (Table 1). It was therefore concluded that these SAFs have an equilibrium thickness [12,13].

(iii) The equilibrium thickness exhibits a reversible dependence on temperature and adsorbate/solute chemical potentials (Fig. 2; Table 1) [13,15]. The film thickness, corresponding to the Gibbsian excess of solute, decreases monotonically with decreasing temperature in the subeutectic range until nearly vanishing at a lower dewetting/drying temperature. With increasing temperature, the films persist into the solid–liquid co-existence regime with gradual thickening upon heating and a complete wetting is expected to occur at higher temperature. The surficial films are thinner in unsaturated specimens containing a lesser concentrations of Bi_2O_3 below the solid-solubility limit.

(iv) While none of the films appear to be fully crystalline, most films exhibit some degree of layering and lateral order [15]. Although some order likely has intensified during the quench, this observation supports the induced-order hypothesis in the original Clarke model [1].

(v) These SAFs have been found to form at thermal equilibration well below the bulk solidus and eutectic temperatures (Figs. 1 and 2(a)). The formation of subeutectic and subsolidus "liquid-like" surficial films was presumed to be driven by the reduction of interfacial energies [12,13], being phenomenologically analogous to theory of surface melting or premelting [24–26].

(vi) Like IGFs in ZnO–Bi_2O_3 [9,10], the nanoscale SAFs are markedly enriched in ZnO, as compared with the equilibrium liquid. The average measured composition of the film formed at 780 °C is 18 mol% Bi_2O_3 [13], while the near-

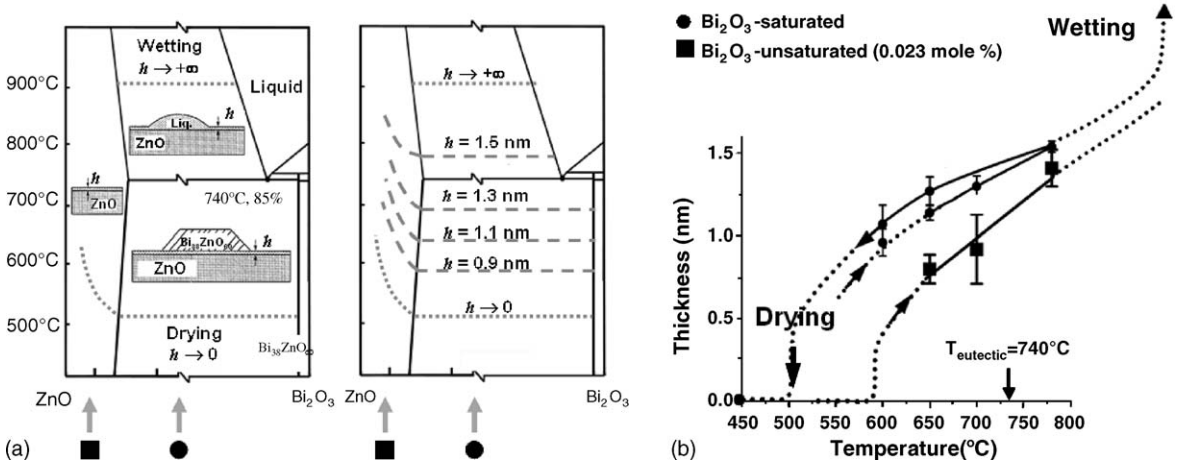

Fig. 2. (a) Schematic illustration of observed Bi_2O_3-enriched SAFs on ZnO $\{1\,1\,\bar{2}\,0\}$ surfaces in the phase regions of the ZnO–Bi_2O_3 binary phase diagram. Lines of constant film thickness, corresponding to constant adsorptions, are indicated. (b) Average thicknesses vs. temperature in saturated and unsaturated samples. For saturated samples, the equilibration was approached from both higher and lower temperatures, demonstrating reversible temperature-dependence of film thickness. The data are taken from Refs. [12–15], and summarized in Table 1.

Table 1
Summary of experimental conditions and corresponding thicknesses of SAFs for Bi_2O_3 on ZnO $\{1\,1\,\bar{2}\,0\}$ surfaces

Samples	Number of observations	Mean thickness (nm) ± standard deviation
Bi_2O_3-saturated, $T > T_{Eutectic}$		
Total (equilibrated at 780 °C)	97	1.54 ± 0.28
ZnO + 0.58 mol% Bi_2O_3, 780 °C, 1 h	48	1.54 ± 0.33
ZnO + 0.58 mol% Bi_2O_3, 780 °C, 2 h	19	1.53 ± 0.20
ZnO + 0.58 mol% Bi_2O_3, 780 °C, 3 h	11	1.47 ± 0.30
ZnO + 1.68 mol% Bi_2O_3, 780 °C, 1 h	19	1.59 ± 0.20
Bi_2O_3-saturated, $T < T_{Eutectic}$		
Approach the equilibrium state from lower temperature		
ZnO + 0.58 mol% Bi_2O_3, 700 °C, 10 h	34	1.30 ± 0.31
ZnO + 0.58 mol% Bi_2O_3, 650 °C, 24 h	29	1.14 ± 0.21
ZnO + 0.58 mol% Bi_2O_3, 600 °C, 24 h	17	0.96 ± 0.28
	9	No films
Approach the equilibrium state from higher temperature		
ZnO + 0.58 mol% Bi_2O_3, 780 °C, 1 h + 650 °C, 24 h	13	1.27 ± 0.26
ZnO + 0.58 mol% Bi_2O_3, 780 °C, 1 h + 600 °C, 96 h	6	1.07 ± 0.22
ZnO + 0.58 mol% Bi_2O_3, 780 °C, 1 h + 450 °C, 6 months	Surface films may dewet.	
Bi_2O_3-unsaturated		
ZnO + 0.023 mol% Bi_2O_3, 780 °C, 24 h	10	1.41 ± 0.29
ZnO + 0.023 mol% Bi_2O_3, 700 °C, 24 h	4	0.92 ± 0.31
ZnO + 0.023 mol% Bi_2O_3, 650 °C, 48 h	5	0.80 ± 0.15

eutectic equilibrium bulk liquid contain ~83 mol% Bi_2O_3 at the same temperature [27].

(vii) A second class of thicker films co-existing with nano-droplets was observed, which indicates that the liquid does not wet the disordered surface layer [15].

The formation of surficial films containing adsorbates at thermal equilibration should obey the Gibbs adsorption theory. The Gibbs isotherm equation, which relates changes in surface energy with surface excess, should apply to the excess energy of the entire SAF represents the excess free energy γ_{cv} for the ZnO surface. However, this thermodynamic relation does not predict all film characteristics, such as thickness or composition. The purpose of this paper is to develop more descriptive theories for SAFs using two approaches: a pressure-balance model extended from the original Clarke model for IGFs [1,2] and a diffuse-interface model extended from Cahn's prewetting and critical wetting model for immiscible liquids [18].

3. Surficial film stability in a pressure-balance model

In a pressure-balance model extended from the original Clarke model for intergranular films [1,2], the excess free energy per unit area associated with the SAF is written as

$$\sigma^x = \gamma_{cl} + \gamma_{lv} - \frac{A_{123}}{12\pi h^2} + E_{struc}(h) + E_{chem}(h) + E_{elec}(h) + (\Delta G_{vol} h), \quad (1a)$$

where γ_{cl} and γ_{lv} are the interfacial energies for the well-separated crystal–liquid and liquid–vapor interfaces, respectively (which are well-defined thermodynamic potentials). The additional terms in Eq. (1a) arise when the crystal–liquid and liquid–vapor interfaces interacts, as a result of the overlap of the external potentials imposed by the adjoining crystal and vapor phases. Here, $\sigma^x \equiv (F^x/A) - \sum_i \mu_i \Gamma_i$ is the most appropriate thermodynamic potential for the system's constraints. In early publications [13,15] G^x was used to represent the excess free energy. However, the excess Helmholtz free energy F^x is a less vague term to use here because the excess Gibbs free energy is defined as $G^x/A \equiv F^x/A - \gamma$ in the convention recommended by the International Union of Pure and Applied Chemistry (IUPAC). Additionally, the inclusion of the reference term $(-\sum_i \mu_i \Gamma_i)$ ensures that σ^x does not depend on the arbitrary position of the Gibbs dividing plane.

The excess film energy as a function of film thickness h, referred to the state of $h = 0$, is a sum of several interactions:

$$\Delta\sigma(h) = \Delta\gamma - \frac{A_{123}}{12\pi h^2} + E_{struc}(h) + E_{chem}(h) + E_{elec}(h) + (\Delta G_{vol} h) \quad (1b)$$

with

$$\Delta\gamma = \gamma_{cl} + \gamma_{lv} - \gamma_{cv}^{(0)} \quad (1c)$$

The first term in Eq. (1b) is the reduction in interfacial free energy upon forming a surficial layer (i.e., replacing the ordered crystal surface with independent liquid surface and crystal–liquid interface). The term $\gamma_{cv}^{(0)}$ refers to the excess free energy for the crystalline surface without an SAF, and the superscript (0) indicates that it differs from γ_{cv}, the excess free energy for the multilayer disordered ZnO surface with equilibrium adsorbates, which should correspond to a minimum of Eq. (1a) with respect to h with no applied stresses. When the film interfaces interact, additional contributions to energy arise. The second term in Eq. (1b) is the non-retarded London dispersion interaction where A_{123} is the Hamaker constant for the system air(1)/film(2)/substrate(3). The terms $E_{struc}(h)$, $E_{chem}(h)$, and $E_{elec}(h)$ are the medium-range

interactions of structural [1,12], chemical [5], and electrostatic [2] origins, respectively, written as independent terms in Eq. (1) for clarity. Finally, ΔG_{vol} is the difference in volumetric Gibbs free energies for a liquid of the equilibrium bulk composition and that of the average film composition. ΔG_{vol} is nonzero when the bulk amorphous phase is metastable (i.e., at temperatures below the below the bulk eutectic temperature) or when the film has an average composition distinct from that of the equilibrium bulk liquid.

However, in principle, the four terms, $E_{struc}(h)$, $E_{chem}(h)$, $E_{elec}(h)$, and ΔG_{vol}, cannot be separated and calculated independently. The sum of these four terms and the dispersion interaction represents one physical quantity, i.e., the change in the excess free energy of the system arising from the finite width of the surficial film as a result of the interaction of the two interfaces. A surficial film of a thickness h for which $\Delta\sigma(h) < 0$ is stable, and the equilibrium thickness corresponds to a (global) minimum excess free energy, for which:

$$\frac{d\,\Delta\sigma(h)}{dh} = 0 \tag{2}$$

$\sigma(h)$ may have multiple minima, but only the global minimum corresponds to the equilibrium surface. In particular, because of the layering of SAFs [15], multiple minima like exist, where each minimum is close (but not necessarily identical) to an integer number of layers (being analogous to the layering transitions in multilayer gas adsorption); a global minimum for a given set of chemical potentials and temperature can correspond to a dry surface (~zero or submonolayer thickness), an equilibrium SAF/moist surface (finite thickness), or a wet surface (infinite thickness).

The spatial derivatives of the interactions in Eq. (1) are equivalent to attractive or repulsive pressures acting across the film. The presence of a long-range attractive dispersion pressure was proposed to be critical to prevent intergranular films from unlimited thickening [1,2]. However, we previously reported [13] the existence of nanometer-thick stable surficial films containing Bi_2O_3 on Fe_2O_3 and WO_3 on TiO_2 where the dispersion interactions are repulsive (i.e., $A_{123} < 0$). Based on this observation combined with numerical evaluation [13], it was, therefore, suggested that ΔG_{vol} is the key attractive interaction below the bulk solidus temperature.

This formulation, however, is inherently imprecise for a nonwetting thin film, in part, as compositional or structural gradients associated with the creation of both the equilibrium solid–liquid and liquid–vapor interfacial configurations may span dimensions comparable to or exceeding an SAF thickness. However, for a situation in which the liquid is nearly perfectly wetting, we can usefully approximate the medium-range interactions (except for dispersion forces) as being largely repulsive and, thereby, elucidate some trends. Thus, we adopt a generic exponentially-decaying form [3] for the medium-range repulsion:

$$E_{\text{medium-range}}(h) = -\Delta\gamma \cdot e^{-h/\xi} \tag{3}$$

which may include structural, chemical, and electrostatic contributions. The two parameters for the medium-range interaction are the reduction of interfacial energies $\Delta\gamma$ and the coherence length ξ. Combining Eqs. (1)–(3), the equilibrium thickness of a surficial film, representing a balance of attractive and repulsive pressures, should satisfy:

$$\frac{A_{123}}{6\pi h^3} + \frac{\Delta\gamma}{\xi} \cdot e^{-h/\xi} + \Delta G_{vol} = 0 \tag{4}$$

To evaluate the thickness versus temperature relation for Bi_2O_3 on ZnO, we can make several estimates. For Bi_2O_3–ZnO eutectic liquid on ZnO, the dispersion interaction is attractive and the Hamaker constant A_{123} was calculated from measured optical properties to be +137 zJ [13]. Since $-\Delta\gamma$ should be greater than zero but less than the difference in crystal and liquid surface energies ($\gamma_{cv} - \gamma_{lv}$) = 500 mJ/m^2 [28], a median value of 250 mJ/m^2 is adopted.

We propose the surficial films in Bi_2O_3-saturated specimens equilibrated slightly above eutectic temperature are represented by the model expressed in Eq. (4) with $\Delta G_{vol} \approx 0$, where the compositional undercooling is ignored for simplicity. Then, for the SAFs formed at 780 °C, the equilibrium thickness associated with a balance of the first two terms in Eq. (4) is taken to be equal to the experimentally measured mean value of 1.54 nm, from which ξ was evaluated to be 0.25 nm. The computed coherence length is close to the typical value (0.3 nm) that was assumed for silicates in previous research [1,3]. The associated excess film free energy versus thickness curve is shown in Fig. 3(a) for the case of no undercooling.

At large undercoolings, the ΔG_{vol} for amorphization will become the dominant term [13]. A one-component formulation based simply on the film-forming additive is used to evaluate the magnitude of this term:

$$\Delta G_{vol}^{amorph} = \Delta S_{fusion}\,\Delta T \tag{5a}$$

where ΔS_{fusion} and ΔT are the fusion entropy and undercooling, respectively. Substituting in the fusion entropy value of pure Bi_2O_3 (0.29 mJ m^{-2} nm^{-1} K^{-1}) [29], the pressures due to the amorphization term are estimated to be 11.6–40.6 MPa at an undercooling of 40–140 K (i.e., 600–700 °C), compared to the dispersion forces being 1.5–5.5 MPa for h of 1.5–1 nm. Then, further assuming, for simplicity, that A_{123}, $\Delta\gamma$, and ξ are effectively independent of temperature in the range of temperatures of interest, the excess film free energies, $\Delta\sigma(h)$, versus thicknesses were computed for several temperatures using Eqs. (1), (3), and (5a), and results are shown in Fig. 3. The equilibrium thicknesses at 600, 650, and 700 °C, respectively, corresponding to the minima as in Fig. 3, are 0.8, 0.9, and 1.1 nm, respectively. These results are 0.1–0.2 nm lower than the experimental data shown in Table 1. This simple model also exhibits a transition at an undercooling of about 300 °C; below this no finite film is stable. This is in good agreement with the observation of a dewetting/drying transition, but underestimates the actual transition temperature. Even with these approximations, the model predicts reasonable equilibrium film thicknesses versus temperature behavior, and suggests that the ΔG_{vol} plays a critical role in determining subeutectic or subsolidus film stability. Below and above this temperature, the deep minimum in $\Delta\sigma(h)$ with a vanishingly thin film, also predicted by the model, is a con-

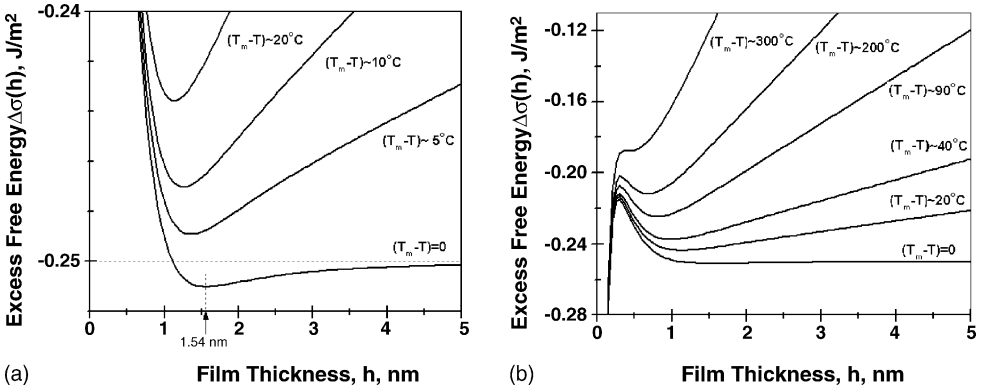

Fig. 3. Computed excess film energies vs. thickness. In (a) for $\Delta T = \Delta G_{vol} = 0$, using $\xi = 0.25$ nm corresponds to an equilibrium thickness of 1.54 nm, representing films equilibrated slightly above the eutectic temperature (at 780 °C). Then, in (a) and (b) excess film free energy vs. thickness curves are shown for temperatures below the solidus temperature down to $\Delta T = 300$ °C, $T \sim 440$ °C.

sequence of the singularity in this continuum description of the dispersion force, $\propto 1/h^3$, and could be eliminated from the model with considerations of finite atomic separations; the minimum near zero is ignored in this heuristic model.

Further consideration suggests that ΔG_{vol} can still be positive because of compositional undercooling at and somewhat above the eutectic temperature. Measured compositions of films co-existing with bulk liquid are markedly different from that of the bulk liquid [13]. This term should depend on film thickness because the average film composition varies (approaching the bulk liquid composition) as the SAF thickness increases. A simple estimate of the associated volume energy can be from

$$\Delta G_{vol}^{amorph} \approx \left(\frac{kT}{V_c}\right) \ln\left(\frac{c}{c_0}\right). \tag{5b}$$

where c is the solute composition in the film, c_0 that in the bulk liquid, and V_c is the volume per cation in each.

Refined models could be developed with better estimates of the interfacial energies and empirical compositions of the SAFs. Further refinements would remove the assumption of a homogenous film composition and structure. The equilibrium composition should derive from a compromise: to minimize the volume penalty, the composition is coerced towards the bulk liquid; to minimize the interfacial transition energy, that the composition would approach that of the bulk substrate; to minimize the short-range excess energy associated with a terminating surface, it approaches that of the surface of the bulk liquid. Through thickness surface film gradients can facilitate in some respects, but energy penalties must be considered explicitly. These are described in the context of diffuse-interface theories discussed in Section 4.

4. Surficial films as a case of prewetting in a diffuse-interface model

The sequence of adsorption and wetting events in Bi_2O_3 on ZnO $\{1\,1\,\bar{2}\,0\}$ facets as a function of temperature and composition may be alternatively interpreted as a case of prewetting, as a generalization of the theory proposed by Cahn for binary immiscible liquids [18] and confirmed for organic and metallic liquids [19–22] and a binary liquid crystal system [23]. A schematic of the phase diagram of the system studied by Cahn is depicted in Fig. 4(a). For Bi_2O_3 on ZnO $\{1\,1\,\bar{2}\,0\}$ surfaces, the film thickness exhibits a temperature dependence counter to that expected from adsorption in the Langmuir–McLean model [30], but consistent with that of the prewetting model [18], in that it decreases monotonically with decreasing temperature in the range below the eutectic at 740 °C until nearly vanishing at a surface dewetting/drying temperature between 450 and 600 °C. A Langmuir-type submonolayer adsorption is expected to occur below the drying temperature. With increasing temperature, the Bi_2O_3-rich films persist well into the solid–liquid co-existence regime. However, perfect wetting of Bi_2O_3-enriched liquid was found to occur on the polycrystalline ZnO surface at ~920 °C [28] and at grain boundaries in Bi_2O_3-doped ZnO at ~950 °C [31]. Thus, perfect wetting may be expected to occur on the $\{1\,1\,\bar{2}\,0\}$ surface above 900 °C. A schematic phase diagram of the observation made for Bi_2O_3 on ZnO is depicted in Fig. 4(b), which is consistent with a generalized prewetting/premelting model proposed in the following text.

There are two distinct transitions (Figs. 2 and 4(b)) in the present case for Bi_2O_3 on ZnO, one for the onset of thick adsorption layers and a second for the transition to complete wetting (i.e., contact angle $\theta = 0$ and $\gamma_{sv} = \gamma_{sl} + \gamma_{lv}$) above which surface films are arbitrarily thick. We call these drying and complete wetting transitions and the intervening region of equilibrium films to correspond to moist surfaces. The dry to moist/SAF transition lines in the subeutectic and subsolidus regimes appear to be the prewetting lines for the present case, which are analogous to the low to high adsorption transition line in the original Cahn model (Fig. 4(a)).

A model for surficial films in Bi_2O_3–ZnO can be obtained as an extension to Cahn's theory [18]. The adsorption in the prewetting regime is analyzed using a diffuse-interface model for the concentration function $c(x)$ that minimizes the excess free energy per unit area of a flat surface:

$$\sigma^x = \Phi(c_s) + \int_0^\infty [\Delta f(c) + \kappa_c \cdot |\nabla c|^2]\, dx \tag{6}$$

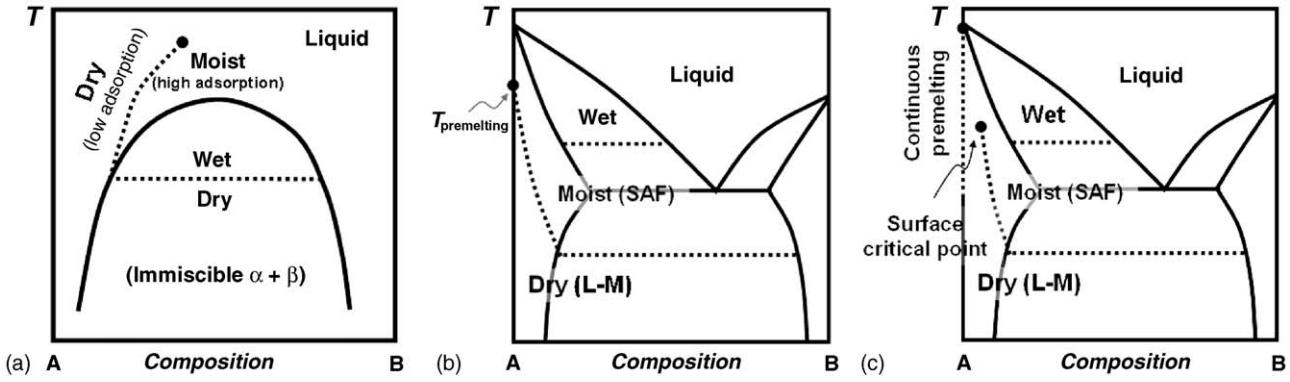

Fig. 4. (a) Schematic illustration of Cahn's prewetting model [18] for binary immiscible liquids, where the complete wetting line in the co-existence regime extends into the single-phase region as a first-order prewetting (low to high adsorption transition) line which terminates at a surface critical point. (b) Schematic illustration of a generalized prewetting model that represents the wetting and adsorption events in ZnO–Bi_2O_3 as shown in Fig. 2. This is one of several possible surface phase diagrams for a two-component system with a bulk eutectic reaction. The moist surfaces correspond to high adsorption or the formation of SAFs. Below the drying temperature, the occurrence of Langmuir–McLean (L–M) type submonolayer adsorption is expected. The prewetting line, representing a first-order transition from L–M adsorption (dry) to SAFs (moist), extends from the subeutectic regime into the single-phase region and terminates at a first-order surface premelting transition point. (c) If the surface premelting transition for the (pure) end member A is continuous (i.e., no first-order thin-thick transition), the prewetting line is expected to terminate at a surface critical point. See text for details.

where x is the spatial parameter, perpendicular to the free surface located at $x=0$; $\Phi(c_s)$ is the short-range excess energy associated with a terminating surface (i.e., surface boundary-condition energy term), where c_s is the concentration at the surface; $\Delta f(c)$ is the homogenous free energy referred to equilibrium bulk phases and a typical $\Delta f(c)$ is schematically illustrated in Fig. 7(a).

The observed surficial films form on crystalline solids and their incomplete ordering is a key attribute in the physics of the film's stability. Based on recent diffuse-interface models for crystal–liquid interfaces being extended to intergranular films [32–35], the prewetting model [18] can be modified to include two order parameters, where the film energy functional is

$$\sigma^x = \Phi(c_s, \eta_s, \theta_s) + \int_0^\infty [\Delta f(\eta, c) + \kappa_\eta |\nabla\eta|^2 + s(\eta)|\nabla\theta| + \kappa_c |\nabla c|^2]\, dx \quad (7)$$

where η and θ are the spatially-varying order parameters of crystallinity and orientation; $\Delta f(\eta, c)$ is a function of both concentration and crystallinity but independent of orientation. Gradient energy coefficients, κ_η, κ_c, and $s(\eta)$, are the model parameters. The surface boundary-condition energy $\Phi(c_s, \eta_s, \theta_s)$ could depend on all three parameters. The gradient in orientation ($\nabla\theta$) is less important for surficial films than that in intergranular films, where a "forced" $\Delta\theta$ is imposed by two boundary conditions, and thus may be neglected for simplicity. Although the gradient and surface boundary-condition terms could depend on the actual surface orientation θ_s, this orientation does not vary spatially if $\nabla\theta \approx 0$. Thus, Eq. (7) can be further simplified for a fixed orientation as:

$$\sigma^x = \tilde{\Phi}(\tilde{c}_s, \tilde{\eta}_s) + \int_0^\infty [\Delta f(\tilde{\eta}, \tilde{c}) + |\nabla\tilde{\eta}|^2 + |\nabla\tilde{c}|^2]\, dx \quad (8a)$$

where the θ_s dependence is omitted and the following normalized field variables are used for brevity:

$$\begin{cases} \tilde{c} = \dfrac{c}{\sqrt{\kappa_c}} \\ \tilde{\eta} = \dfrac{\eta}{\sqrt{\kappa_\eta}} \end{cases} \quad (8b)$$

The effects of dispersion forces, electrical double-layer space-charge, and strain energy should be included separately but are not developed here.

The equilibrium spatially-varying $\tilde{\eta}(x)$ and $\tilde{c}(x)$ profiles correspond to the global minimum in the excess free energy expressed in Eq. (8a), which, from Appendix A, should satisfy:

$$|\nabla\tilde{\eta}(x)|^2 + |\nabla\tilde{c}(x)|^2 = \Delta f(\tilde{\eta}, \tilde{c}) \quad (9)$$

Also from Appendix A, Eq. (8a) can be transformed to an equivalent variational calculus problem in the $(\tilde{c}, \tilde{\eta})$-space using Eq. (9). Thus, the excess surface free energy referred to an unrelaxed, cleaved surface (i.e., a refined expression for $\Delta\sigma$ in Eq. (1b) considering through-thickness gradients) is found to be:

$$\Delta\sigma = -\Delta\tilde{\Phi}(\tilde{c}_s, \tilde{\eta}_s) + I(\tilde{c}_s, \tilde{\eta}_s) \quad (10a)$$

The first term, the reduction in the surface boundary-condition energy term due to concentration and structure variations at the terminating surface, is the primary driving force for surface adsorption and/or disordering:

$$\Delta\tilde{\Phi}(\tilde{c}_s, \tilde{\eta}_s) \equiv \tilde{\Phi}(\tilde{c}_b, \tilde{\eta}_b) - \tilde{\Phi}(\tilde{c}_s, \tilde{\eta}_s) > 0 \quad (10b)$$

The second term in Eq. (10a) represents the total volumetric and gradient energies, which is an energy penalty for the near-surface variations in concentration and order parameter. This term is a path integral in the $(\tilde{c}, \tilde{\eta})$-space:

$$I(\tilde{c}_s, \tilde{\eta}_s) = \int_{(\tilde{c}_b, \tilde{\eta}_b)}^{(\tilde{c}_s, \tilde{\eta}_s)} \left[2\sqrt{\Delta f(\tilde{\eta}, \tilde{c})}\right] ds \quad (10c)$$

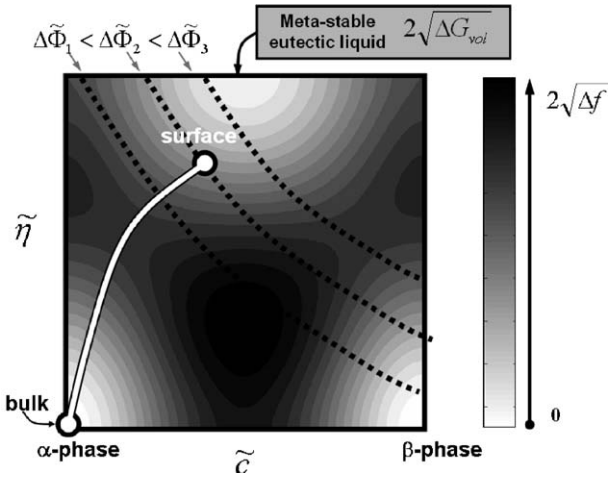

Fig. 5. A graphic interpretation of the diffuse-interface formulation expressed in Eq. (10). The contours of a representative $2\sqrt{\Delta f(\tilde{\eta}, \tilde{c})}$ in the subeutectic region are plotted in gray scale in the $(\tilde{c}, \tilde{\eta})$-space. Simultaneous variation in concentration and order parameter from inside the bulk material to the free surface is shown as the white line. Three contours of $\Delta\tilde{\Phi}$ are plotted as the dotted lines. Since $\Delta\sigma = -\Delta\tilde{\Phi} + I$ (Eq. (10)), the surface concentration $(\tilde{c}_s)$ and order parameter $(\tilde{\eta}_s)$ are derived by a compromise: The $-\Delta\tilde{\Phi}$ term drives $(\tilde{c}_s, \tilde{\eta}_s)$ to be away from, while I, the path integral of $2\sqrt{\Delta f}$ along the white line, "pulls" them back to, the bulk values $(\tilde{c}_b, \tilde{\eta}_b)$.

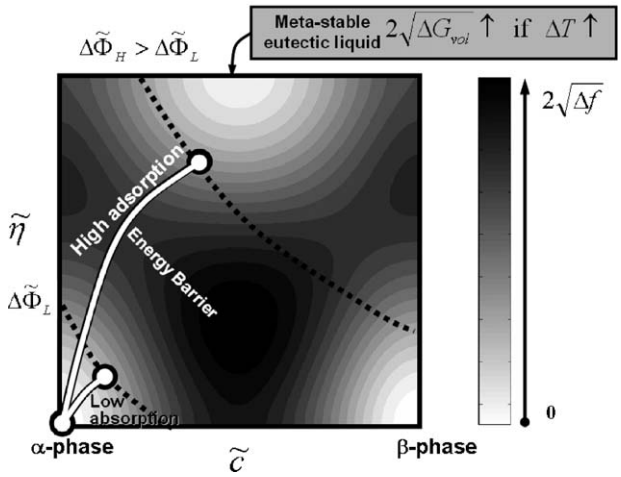

Fig. 6. Schematic illustration of a first-order prewetting/drying/dewetting transition. Due to the existence of an energy barrier, two local minima should exist for $\Delta\sigma = -\Delta\tilde{\Phi} + I$. Assuming that the high adsorption configuration has lower $\Delta\sigma$ near the bulk eutectic temperature, moist surfaces, or SAFs are thermodynamically stable. As the temperature deceases in the subeutectic region $(\Delta T\uparrow)$, the path integral for high adsorption I_H increases significantly with increasing ΔG_{vol} for the metastable liquid phase, leading to drying transition where the low adsorption state becomes energetically preferred.

Here $(\tilde{c}_b, \tilde{\eta}_b)$ and $(\tilde{c}_s, \tilde{\eta}_s)$ are the normalized concentration and order parameter inside the bulk material and at the surface, respectively. The integration path in Eq. (10c) should be chosen to minimize the integral $I(\tilde{c}_s, \tilde{\eta}_s)$ for any given pair of $(\tilde{c}_s, \tilde{\eta}_s)$.

Eq. (10) provides a graphical construction for equilibrium solutions to the diffuse-interface model. The contours of $2\sqrt{\Delta f}$ are plotted in gray scale in the $(\tilde{c}, \tilde{\eta})$-space in Fig. 5, where the simultaneous variation in $\tilde{c}$ and $\tilde{\eta}$ from inside the bulk material to the surface is shown as the white line with two open dots representing the bulk material and the surface. $I(\tilde{c}_s, \tilde{\eta}_s)$, an energy penalty for compositional and structural variations near the surface, is represented by a path integral of the function $2\sqrt{\Delta f}$ along the white line in Fig. 5. Three contours of $\Delta\tilde{\Phi}$ are also plotted as the dotted lines in Fig. 5, assuming adsorption and surface disordering reduces the surface term $\Delta\tilde{\Phi}$. Surface adsorption and disordering are driven by the $-\Delta\tilde{\Phi}(\tilde{c}_s, \tilde{\eta}_s)$ term, at the expense of an increase in the path integral $I(\tilde{c}_s, \tilde{\eta}_s)$. The surface concentration $(\tilde{c}_s)$ and order parameter $(\tilde{\eta}_s)$ are therefore derived by a compromise between the two terms. The thermodynamic equilibrium surface configuration corresponds to the $(\tilde{c}, \tilde{\eta})$ trace (i.e., a white line in Fig. 5) that minimizes the total excess energy expressed in Eq. (10a). The spatial dependences of concentration $\tilde{c}(x)$ and order parameter $\tilde{\eta}(x)$ can be then obtained using Eq. (9) for a given $(\tilde{c}, \tilde{\eta})$ trace.

First-order dry to moist/SAF transitions can be deduced graphically (Fig. 6). This type of transitions is termed drying, dewetting, or prewetting transition, and we use these three terms interchangeably. Due to the existence of an energy barrier in excess volumetric free energy Δf, and correspondingly in the contours of $2\sqrt{\Delta f}$, two local minima should exist for $\Delta\sigma$ expressed in Eq. (10a), one for low adsorption (small $\Delta\Phi_L$ and I_L) and one for high adsorption (large $\Delta\Phi_H$ and I_H). If the driving force for adsorption, $\Delta\Phi$, is significant, the high adsorption state is energetically preferred near the bulk eutectic temperature and the low adsorption is metastable. As the temperature deceases in the subeutectic region $(\Delta T\uparrow)$, the path integral for high adsorption, I_H, increases with increasing ΔG_{vol} for the metastable liquid phase, leading to a transition where the low adsorption configuration becomes energetically favorite. The first-order drying/dewetting transition (i.e., the prewetting) temperature is therefore defined by

$$\Delta G_H = -\Delta\tilde{\Phi}_H + I_H = \Delta G_L = -\Delta\tilde{\Phi}_L + I_L \quad (11)$$

Analysis of the KWC model [32] also suggested the existence of similar first-order prewetting transitions for grain boundaries [35].

The prewetting/drying line should extend into the single-phase regime, where the prewetting/drying temperature increases with decreasing chemical potential. The prewetting/drying line may terminate at either a first-order surface premelting transition point (Fig. 4(b)) if the end member A does exhibit a first-order premelting transition, or a surface critical point (Fig. 4(c)) if the surface of the end member A does not premelt or premelts as a continuous transition. Assuming a double-well potential [36] for the $\tilde{\eta}$ dependence of excess volumetric free energy Δf, the energy barrier (as schematically shown in Fig. 6), if high enough, likely persists throughout the entire single-phase regime, suggesting the possibility for the existence of a first-order premelting transition point (Fig. 4(b)).

The occurrence of complete wetting is more complicated for the present case. According to Eq. (9), complete wetting occurs under the condition that the white line in Fig. 5 or Fig. 6 passes through a point of zero volumetric free energy (that corresponds

to an equilibrium liquid), wherein

$$|\nabla\tilde{\eta}(x)|^2 + |\nabla\tilde{c}(x)|^2 = \Delta f = 0 \tag{12}$$

indicates a thick (bulk) film with constant $\tilde{c}(x)$ and $\tilde{\eta}(x)$. Dependent on the specific formulation of $\Delta\tilde{\Phi}(\tilde{c}_s, \tilde{\eta}_s)$ and $\Delta f(\tilde{c}, \tilde{\eta})$, complete wetting may either occur at the bulk eutectic temperature or be delayed to a higher temperature. In other words, compositional undercooling and/or coupling between the volumetric and gradient terms in Eq. (8a) may, but need not, result in an effective attractive pressure that prevents/delays the divergence of film thickness at the bulk eutectic temperature. The existence of additional attractive interactions that are not included in the diffuse-interface model, such as the London dispersion force, likely further delays complete wetting.

Based on the above discussions, two possible surface prewetting/premelting phase diagrams are assembled in Fig. 4(b and c), which resemble the observation made for Bi_2O_3 on ZnO as shown in Fig. 2. It is worthy noting that Fig. 4(b and c) only represent two of many possible surface phase diagrams that can be deduced for Eq. (10) for different Δf and $\Delta\tilde{\Phi}$ functions. For examples, with a different set of Δf and $\Delta\tilde{\Phi}$ functions, (1) the complete wetting may occur at the bulk eutectic temperature where the film thickness is divergent, (2) the drying and complete wetting transitions may merge into one horizontal line in the liquid–solid co-existence regime, and (3) solid-state wetting and/or ordered multilayer adsorbates may also occur. A systematic assessment of all types of surface prewetting/premelting phase diagrams is beyond the scope of this paper.

The prewetting/premelting model can also be qualitatively adjusted to correlate with experimental observations. For example, the film–substrate interface in Fig. 1 is nearly atomically abrupt, appearing to contradict the "diffuse interface" results predicted by Cahn's original prewetting model [18]. Such a qualitative difference in behavior might well be expected from different bulk phase diagrams: one with a deep eutectic reaction (Fig. 4(b)) versus a binary liquid with a miscibility gap (Fig. 4(a)). From Eq. (7) in Ref. [18] the concentration gradient at the adsorbate–substrate transition is

$$\left|\frac{dc}{dx}\right|_{trans} = \sqrt{\frac{\Delta E}{\kappa_c}} \tag{13a}$$

where ΔE is the height of the barrier between substrate and film in the free energy versus concentration function (being schematically illustrated in Fig. 7). In the present system (ZnO–Bi_2O_3), the free energy barrier for the structural transition is very high and would be consistent with a region of atomically-abrupt film–substrate transition between graded regions in the film and perhaps in the crystalline substrate. The more accurate formulation for surficial films can be deduced from Eq. (9) including both concentration and order parameters as a generalization Eq. (13a):

$$\sqrt{\left|\frac{d\tilde{\eta}}{dx}\right|^2_{trans} + \left|\frac{d\tilde{c}}{dx}\right|^2_{trans}} = \sqrt{\Delta E} \tag{13b}$$

where a similar analysis can be proposed. The existence of an abrupt transition would also support contemplation of the simplified treatment of the film free energy model in Section 3 where through-thickness gradients are neglected, but for approximations concerning medium-range forces.

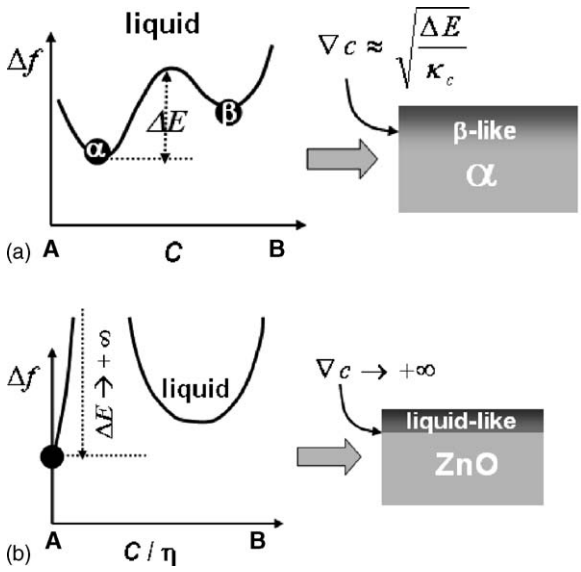

Fig. 7. The diffuse vs. abrupt adsorbate–substrate interfaces can also be understood through differing volumetric free energy functions associated with the bulk phase diagrams.

5. General discussion

The pressure-balance formulation provides useful insights, but provides no microscopic physical interpretation for the various contributions to interfacial pressure (i.e., it treats the film as homogenous and incapable of forming adsorption layers). A simple interpretation would suppose the ordered crystal surface to be clean (without any adsorption), and so $\gamma_{cv}^{(0)}$ to be that for a pure crystal. Such an approximation has been invoked for some organic systems [37], but is unlikely, in general, as some adsorption could be expected, which would lower $\gamma_{cv}^{(0)}$ at solute chemical potentials below that for stable film formation. The formulation in Eq. (1a) does not depend on $\gamma_{cv}^{(0)}$, and so Eq. (3) could be reformulated with an approximation to $\Delta\gamma$. However, any adsorption would influence the drying transition condition; moreover, predictions of stable SAF satisfying Eq. (2) may be metastable surface configurations with higher energy than some more ordered surface with a $\gamma_{cv}^{(0)}$ decreased by adsorption.

Although SAFs observed for Bi_2O_3 on ZnO exhibit some evidence of partial order [15], there must be some entropy from structural disorder or compositional mixing in the films to account for the trends in temperature and chemical potential dependences to film thickness. These trends in film thickness, as well as the observed sequence for appearance/disappearance of dry, moist, and wet surfaces as a function of temperature and composition, are predicted by the pressure-balance and diffuse-interface models. The reasonable agreements between the experiments and model predictions, including the quantitative agreement between the calculated and measured thickness versus temperature, support the proposed models, and in par-

ticularly, further supports our prior hypothesis [13,15] of the critical role of volumetric term in determining the surficial film thickness and stability.

Both the pressure-balance model and the diffuse-interface model predict the existence of two distinct transitions (different from the original Cahn model). In subeutectic films, the finite thickness is largely set by the volumetric energy for amorphization. In the pressure-balance model, the presence of the dispersion force causes an abrupt drying transition, and it is the only explicit force in that model that delays complete wetting when $\Delta G_{\mathrm{vol}} \approx 0$; without it, Eqs. (5) give $h_{\mathrm{eq}} \propto -\ln(\Delta T/T_{\mathrm{m}})$, i.e., diverging at the melting point, and a continuous drying transition. However, it is not yet experimentally proven that the drying transition is first-order and the eutectic liquid is perfectly wetting but for dispersion forces.

On the other hand, the generalized prewetting diffuse-interface model proposed in Section 4 suggested a first-order drying transition as well as the possibility of a delayed complete wetting even without the attractive dispersion pressure. In addition, the existence of attractive/repulsive dispersion and/or other pressures that are not included in the diffuse-interface model would affect characteristics of the wetting and drying transitions. Along with dispersion forces, epitaxial coherence between the first layer of the SAF and solid surface may be necessary for formation of these films; this would account for lower γ_{cl}, or lower gradient energy penalty terms, but may also imply a structure is imposed onto the SAF that differs from the liquid and prevents perfect wetting.

Numerous microscopic phenomena affect the character of dry, moist, and wet surfaces as well as transitions. Prediction of the characteristic prewetting/premelting phase diagrams requires that each phenomenon be treated. Rich behavior may be expected given that surface reconstruction, film composition, induced partial order, strain and electrostatic energies, and phase separation within the film plane, are all coupled. It may be that interfacial phase diagrams are even more diverse than bulk phase diagrams.

6. Conclusions

The adsorption and wetting events in oxide systems represented by Bi_2O_3 on ZnO can be interpreted as a case of combined prewetting and premelting. However, surficial amorphous films on crystalline solids in two-component oxides with deep eutectic reactions should exhibit different character than adsorption in simpler binary liquids, including for example an atomically abrupt rather than diffuse crystal–film transition. A pressure-balance model with the volumetric free energy being the dominant temperature-dependent interaction results in thicknesses versus temperature behavior for subsolidus films that is in good agreement with experimental results, thereby illustrating the critical role of volumetric free energy term for amorphization in determining subeutectic film stability. Dispersion forces are one, but perhaps not the only force that delays complete wetting. Both pressure-balance model and the generalized prewetting/diffuse-interface model predict the possibility for distinct drying and wetting transitions with the intervening region of equilibrium multilayer adsorbates. Dependent on the specific characteristics of the excess volumetric free energy function and surface boundary-condition energy term as well as the existence and strength of additional interactions such as dispersion pressure, space-charge, and strain energy, a variety of characteristic surface phase diagrams and transitions can exist.

Acknowledgements

Y.M.C., M.T., and W.C.C. acknowledge support from NSF/EU NANOAM collaboration (NSF DMR-0010062, EUG5RD-CT-2001-00586). R.M.C. acknowledges DOE contract No. DE-AC03-76SF00098, and J.L. acknowledges support from Clemson University and an NSF CAREER award (DMR-0448879). Authors thank the critical comments from Prof. Adrian P. Sutton.

Appendix A. Deduction of Eqs. (9) and (10) from Eq. (8)

Using the basic principles of variational calculus, the Euler equations for Eq. (8a) are found to be

$$\begin{cases} \dfrac{\delta(\Delta f)}{\delta\tilde{\eta}} = 2\dfrac{\mathrm{d}^2\tilde{\eta}}{\mathrm{d}x^2} \\ \dfrac{\delta(\Delta f)}{\delta\tilde{c}} = 2\dfrac{\mathrm{d}^2\tilde{c}}{\mathrm{d}x^2} \end{cases} \tag{A.1}$$

Hence:

$$\begin{aligned} \frac{\mathrm{d}(\Delta f)}{\mathrm{d}x} &= \frac{\delta(\Delta f)}{\delta\tilde{\eta}}\cdot\frac{\mathrm{d}\tilde{\eta}}{\mathrm{d}x} + \frac{\delta(\Delta f)}{\delta\tilde{c}}\cdot\frac{\mathrm{d}\tilde{c}}{\mathrm{d}x} \\ &= 2\cdot\frac{\mathrm{d}^2\tilde{\eta}}{\mathrm{d}x^2}\cdot\frac{\mathrm{d}\tilde{\eta}}{\mathrm{d}x} + 2\cdot\frac{\mathrm{d}^2\tilde{c}}{\mathrm{d}x^2}\cdot\frac{\mathrm{d}\tilde{c}}{\mathrm{d}x} \\ &= \frac{\mathrm{d}}{\mathrm{d}x}\left(\left(\frac{\mathrm{d}\tilde{\eta}}{\mathrm{d}x}\right)^2 + \left(\frac{\mathrm{d}\tilde{c}}{\mathrm{d}x}\right)^2\right) \\ &= \frac{\mathrm{d}}{\mathrm{d}x}(|\nabla\tilde{\eta}(x)|^2 + |\nabla\tilde{c}(x)|^2) \end{aligned} \tag{A.2}$$

Integrating the both sides of Eq. (A.2) gives:

$$|\nabla\tilde{\eta}(x)|^2 + |\nabla\tilde{c}(x)|^2 = \Delta f(\tilde{\eta},\tilde{c}) + C_0 \tag{A.4}$$

The constant C_0 should be zero since the following relation should be held inside the bulk material:

$$|\nabla\tilde{\eta}(x)|^2 + |\nabla\tilde{c}(x)|^2 = \Delta f(\tilde{\eta}_{\mathrm{b}},\tilde{c}_{\mathrm{b}}) = 0 \tag{A.5}$$

Thus, Eq. (9) has been deduced.

Using Eq. (9), we can transform variables for the two integrals in Eq. (8a) and (10a) between x-space and $(\tilde{\eta},\tilde{c})$-space:

$$\begin{aligned} &\int_0^\infty [\Delta f(\tilde{\eta},\tilde{c}) + |\nabla\tilde{\eta}|^2 + |\nabla\tilde{c}|^2]\,\mathrm{d}x \\ &= \int_0^\infty 2\cdot\sqrt{\Delta f(\tilde{\eta},\tilde{c})}\cdot\sqrt{|\nabla\tilde{\eta}|^2 + |\nabla\tilde{c}|^2}\,\mathrm{d}x \\ &= \int_{(\tilde{c}_{\mathrm{b}},\tilde{\eta}_{\mathrm{b}})}^{(\tilde{c}_{\mathrm{s}},\tilde{\eta}_{\mathrm{s}})} \left[2\sqrt{\Delta f(\tilde{\eta},\tilde{c})}\right]\,\mathrm{d}s \end{aligned} \tag{A.6}$$

where the following relation is used:

$$\sqrt{|\nabla\tilde{\eta}|^2 + |\nabla\tilde{c}|^2}\,\mathrm{d}x = \sqrt{(\mathrm{d}\tilde{\eta})^2 + (\mathrm{d}\tilde{c})^2} = \mathrm{d}s \tag{A.7}$$

Therefore, the variational calculus problem specified by Eq. (8a) can be equivalently defined by Eqs. (10) and (9).

References

[1] D.R. Clarke, J. Am. Ceram. Soc. 70 (1987) 15–22.
[2] D.R. Clarke, T.M. Shaw, A.P. Philipse, R.G. Horn, J. Am. Ceram. Soc. 76 (1993) 1201–1204.
[3] R.M. Cannon, L. Esposito, Z. Metallkd. 90 (1999) 1002–1015.
[4] H.-J. Kleebe, M.K. Cinibulk, R.M. Cannon, M. Rühle, J. Am. Ceram. Soc. 76 (1993) 1969–1977.
[5] M. Bobeth, D.R. Clarke, W. Pompe, J. Am. Ceram. Soc. 82 (1999) 1537–1546.
[6] P.F. Becher, G.S. Painter, E.Y. Sun, C.H. Hsueh, M.J. Lance, Acta Mater. 48 (2000) 4493–4499.
[7] Y.-M. Chiang, L.A. Silverman, R.H. French, R.M. Cannon, J. Am. Ceram. Soc. 77 (1994) 143–152.
[8] H. Wang, Y.-M. Chiang, J. Am. Ceram. Soc. 81 (1998) 89–96.
[9] Y.-M. Chiang, H. Wang, J.-R. Lee, J. Microscopy 191 (1998) 275–285.
[10] J. Luo, H. Wang, Y.-M. Chiang, J. Am. Ceram. Soc. 82 (1999) 916.
[11] J. Luo, V.K. Gupta, D.H. Yoon, H.M. Meyer III, Appl. Phys. Lett. 87 (2005) 231902.
[12] J. Luo, Y.-M. Chiang, J. Eur. Ceram. Soc. 19 (1999) 697–701.
[13] J. Luo, Y.-M. Chiang, Acta Mater. 48 (2000) 4501–4515.
[14] J. Luo, Ph.D. Thesis, M.I.T., Cambridge, MA, 2001.
[15] J. Luo, Y.-M. Chiang, R.M. Cannon, Langmuir 21 (2005) 7358–7365.
[16] A. Ramos, M. Tang, S.-Y. Chung, R.M. Cannon, Y.-M. Chiang, unpublished work.
[17] R. Pandit, M. Schick, M. Wortis, Phys. Rev. B 26 (1982) 5112.
[18] J.W. Cahn, J. Chem. Phys. 66 (1977) 3667.
[19] J.W. Schmidt, M.R. Moldover, J. Chem. Phys. 84 (1986) 4563.
[20] D. Chatain, P. Wynbalatt, Surf. Sci. 345 (1996) 85–90.
[21] P. Wynbalatt, D. Chatain, Ber. Bunsenges. Phys. Chem. 102 (1998) 1142–1150.
[22] H. Kellay, D. Bonn, J. Meunier, Phys. Rev. Lett. 71 (1993) 2607–2610.
[23] B. Lucht, C. Bahr, Phys. Rev. Lett. 80 (1998) 3783–3786.
[24] J.W.M. Frenken, P.M. Maree, J.F. van der Veen, Phys. Rev. B 34 (1986) 7506.
[25] J.G. Dash, Contemporary Phys. 30 (1989) 89–100.
[26] J.G. Dash, H. Fu, J.S. Wettlaufer, Rep. Prog. Phys. 58 (1995) 115–167.
[27] G.M. Safronov, V.N. Batog, T.V. Stepanyuk, P.M. Fedorov, Russ. J. Inorg. Chem. 16 (1971) 460–461.
[28] J.-G. Li, J. Mater. Sci. Eng. Lett. 13 (1994) 400–403.
[29] G.V. Samsonov, The Oxide Handbook, second ed., Plenum Data Company, New York, 1982.
[30] J.G. Dash, Films on Solid Surfaces: The Physics and Chemistry of Physical Adsorption, Academic Press, New York, 1975.
[31] J.-R. Lee, Y.-M. Chiang, unpublished work.
[32] R. Kobayashi, J.A. Warren, W.C. Carter, Physica D 119 (1998) 415.
[33] A.E. Lobkovsky, J.A. Warren, Physica D 164 (2002) 202–212.
[34] C.M. Bishop, R.M. Cannon, W.C. Carter, Acta Mater. 53 (2005) 4755–4764.
[35] M. Tang, W.C. Carter, R.M. Cannon, unpublished work.
[36] W.J. Boettinger, J.A. Warren, C. Beckermann, A. Karma, Annu. Rev. Mater. Res. 32 (2002) 163–194.
[37] F. Brochard-Wyart, J.-M. di Meglio, D. Quéré, P.G. de Gennes, Langmuir 7 (1991) 335–338.